energies

MDPI

Article

MnO/Mn_2O_3 Aerogels as Effective Materials for Supercapacitor Applications

Ramya Ramkumar †, Sanjeevamuthu Suganthi †, Ahamed Milton, Jungbin Park, Jae-Jin Shim, Tae Hwan Oh * and Woo Kyoung Kim *

School of Chemical Engineering, Yeungnam University, Gyeongsan 38541, Gyeongbuk, Republic of Korea; ramya.iitm@gmail.com (R.R.); suganthichempower@gmail.com (S.S.); miltonahamedru@gmail.com (A.M.); ckrgkswjdqls@naver.com (J.P.); jjshim@yu.ac.kr (J.-J.S.)

* Correspondence: taehwanoh@ynu.ac.kr (T.H.O.); wkim@ynu.ac.kr (W.K.K.)

† These authors contributed equally to this work.

Abstract: Mixed-oxide transition-metal aerogels (AGLs), particularly manganese-based AGLs, have attracted considerable interest over the past decade owing to their extraordinary properties, including high porosity, good surface area, and ultralow density. To develop easy and lightweight materials for the ever-increasing energy storage demands of the near future, we designed a novel Mn-based electrode material to meet these rising requirements. MnO/Mn_2O_3 AGLs were synthesized using a novel borohydride hydrolysis method and then annealed at 200, 400, and 550 °C. The as-synthesized AGLs yielded flower-like network structures, but their porosity increased with increasing temperatures, to a high temperature of 400 °C. This increased porosity and network structure facilitate a high capacitance. A supercapacitor (SC) constructed with the three-electrode material yielded 230 F/g for the Mn_{AGL}@400 sample, followed by yields from the Mn_{AGL}@200 and Mn_{AGL}@550 electrodes. Furthermore, the device constructed with Mn_{AGL}@400 exhibited an energy density of 9.8 Wh/kg and a power density of ~16,500 W/kg at a current density of 20 A/g. The real-time applicability of the AGL was demonstrated by engineering a two-electrode device employing Mn_{AGL}@400 as the positive electrode, which exhibited 97% capacity retention and 109% Coulombic efficiency over 20,000 cycles.

Keywords: supercapacitor; ultra-low densities; energy storage; borohydride hydrolysis; manganese aerogels

check for updates

Citation: Ramkumar, R.; Suganthi, S.; Milton, A.; Park, J.; Shim, J.-J.; Oh, T.H.; Kim, W.K. MnO/Mn_2O_3 Aerogels as Effective Materials for Supercapacitor Applications. *Energies* **2024**, *17*, 2258. https://doi.org/10.3390/en17102258

Academic Editors: Claudio Gerbaldi, Cataldo Simari, Francesca Soavi, Federico Poli, Akiko Tsurumaki and Alessandro Piovano

Received: 4 April 2024
Revised: 26 April 2024
Accepted: 6 May 2024
Published: 8 May 2024

1. Introduction

The ever-increasing demand for energy production and storage and the need for renewable energy storage devices has necessitated the development of new electrode materials. Currently, a large portion of the energy demand is fulfilled by fossil fuels (almost 80%), with the rest covered by nuclear energy, solar cells, batteries, and supercapacitors (SCs) [1]. However, the increasing deficiency of fossil fuels and their imminent danger to global warming and climate change have necessitated exploring areas with more-sustainable, eco-friendly, and low-cost materials [2]. In this regard, capacitors are preferred owing to their high power density and energy density, long cycling stability, fast charge/discharge, low cost, easy handling, and environmental friendliness [2]. SCs or ultracapacitors are more advantageous than batteries because they can deliver high power in the short term with a reasonable energy density [3].

Several materials, including transition metals and their oxides, have been employed in the construction of SCs over the past few decades [4]. Among transition metals, several researchers have studied the effects of Mn and its sulfides or oxides [5]. Several modifications, such as varying the methods of synthesis (such as hydrothermal, CVD, electrodeposition, and sol–gel), structural modifications (such as cylinder, wire, tube, and cones) [6], or the

addition of external enhancement agents to improve activity (such as polymer, CNTs, and graphene) have been proposed. Manganese is the preferred material for electrochemical and energy applications owing to its low cost, abundance in the Earth's crust, enhanced potential window exhibiting high energy densities, environmentally friendly nature, and high theoretical capacity [7,8]. Manganese exhibits several stable oxidation states, such as MnO, MnO_2, Mn_2O_3, and Mn_3O_4, which possess varied electrochemical properties [9]. Manganese also exhibits intercalation and deintercalation of electrolyte ions in the electrode material owing to the transition between Mn^{4+}/Mn^{3+} ions, which leads to enhanced charge storage properties [10]. The various methods used to produce MnO/Mn_2O_3 include hydrothermal methods, thermal decomposition, pulsed laser deposition, microemulsion, template synthesis, wet chemical methods, electrodeposition, and sol–gel synthesis [11–13]. Among these methods, the sol–gel method is of great significance in terms of simplicity and cost-effectiveness [14,15]. In this study, we employed a borohydride hydrolysis sol–gel synthesis route to produce networked MnO/Mn_2O_3 aerogels (AGLs).

Several Mn-based systems have been synthesized for energy storage in SC applications. Xu et al. synthesized carbon AGLs modified with Mn_2O_3 and dimethyl formamide and achieved a specific capacitance of 100 F/g at a current density of 10 A/g, yielding a power density of 3000 W/kg at 0.5 A/g [16]. Chen et al. synthesized nitrogen-doped carbon AGLs modified with Mn_2O_3 and cellulose nanofibrils, which yielded a specific capacitance of 275 F/g at a current density of 1 A/g [17]. Guo et al. reported a mixed AGL with carbon nanocellulose fibers and MnOx that yielded a specific capacitance of 269 F/g at a scan rate of 5 mV/s [18]. Qiu et al. synthesized a graphene AGL MnO_2 composite using a hydrothermal method, yielding a specific capacitance of 63 F/g at a current density of 1 A/g [19]. Xu et al. improved the pore structure of carbon AGLs with a specific capacitance of 186 F/g by introducing Mn ions [20]. Chen et al. reported a superior capacitance of Mn_2O_3 of 225 F/g in comparison with other manganese oxides, owing to the Mn^{3+}/Mn^{2+} and Mn^{4+}/Mn^{3+} transitions occurring during the redox reactions [21]. The self-assembly of mesoporous nanotubes assembled from interwoven ultrathin birnessite by Huang et al. yielded a specific capacitance of 243 F/g [22]. Sun et al. produced Ag nanoparticles decorated with hybrid manganese oxide nanostructures for SC applications, yielding a specific capacitance of 154 F/g at a current density of 1 A/g [23]. Binny et al. reported that using carbon-dot-decorated graphene nanosheets and manganese oxide-based SCs yielded a good capacitance of 280 F/g at 1 A/g [24]. The MnO_2-AGL-composite-based SC yielded a specific capacitance of 333 F/g at a current density of 1 A/g [25]. MnO_2 nanosheets and N-doped graphene AGL yielded a specific capacitance of 467 F/g at a current density of 1 A/g [26]. A MnO_x/rGO_{ae}-AGL-based SC yielded a specific capacitance of 240 F/g at a current density of 0.5 A/g [27].

In this study, we employed a sodium borohydride reducing agent that, when dissolved in water, formed many hydroxyborohydride intermediates which act as mild reducing agents. However, when dissolved in hydroxylic solvents such as ethanol, propanol, or methanol, the same reaction is retarded [28]. In this research, we utilized this feature of borohydrides and introduced them into an ethanolic medium to slow down the reactivity and formation of intermediates, which effectively reduced the manganese salts to manganese hydrogels with the growth of excess hydrogen bubbles owing to the excess of reducing agent present in the reaction. The combined effect of slowed-down hydrolysis and the evolution of hydrogen bubbles led to the formation of lightweight and airy hydrogels, which, when freeze-dried, retained the network structures typically found in AGLs.

AGLs are a unique class of material owing to their light weight, high porosity, and large surface area. Consequently, they are preferred candidates for energy applications, especially in portable electronics, and within the aerospace industry. In this study, we effectively synthesized manganese AGLs using a simple borohydride hydrolysis method to yield MnO/Mn_2O_3 with high activities. This material was further modified by annealing the AGLs at various temperatures and used for SC applications. Mn_{AGL}@400 exhibited the highest specific capacitance of all the electrodes, with a value of 230 F/g at a current

density of 1 A/g. This electrode was further incorporated into an SC device and was found to be a suitable material for lightweight energy storage applications. Scheme 1 shows a graphic representation of the synthesis method for Mn_{AGLs} and their SC performance.

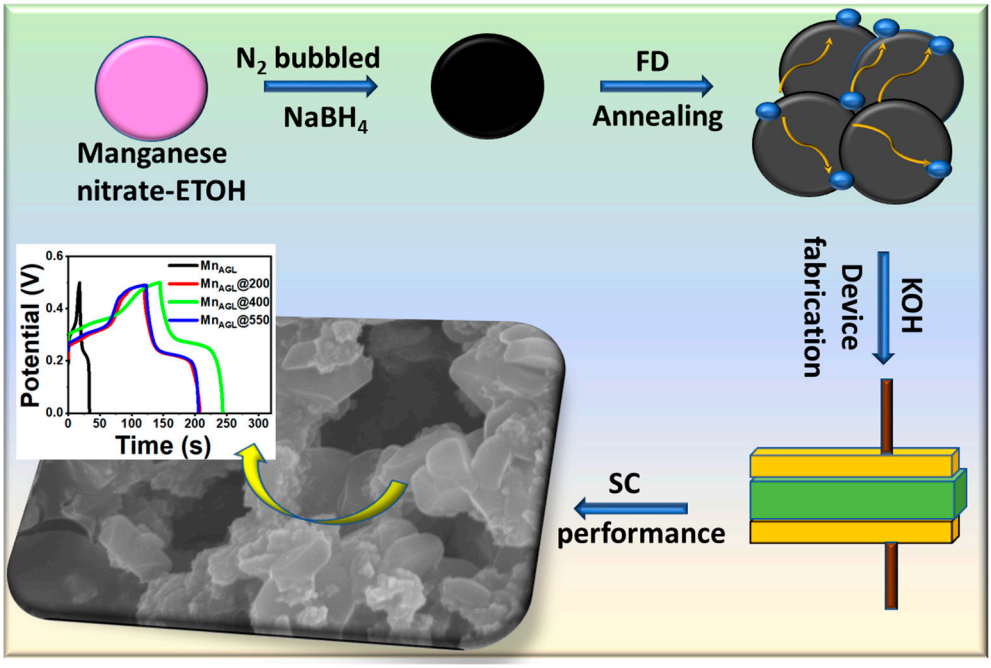

Scheme 1. Schematic of the synthesis method for Mn_{AGLs} and their SC performance.

2. Experimental

A list of the chemicals used in this study and the complete synthesis procedure of the AGLs, along with the characterizations involved, are provided in the Electronic Supplementary Material.

2.1. Electrochemistry

The performance of any energy device, including batteries or SCs, is measured by employing several techniques, such as cyclic voltammetry (CV), galvanostatic charge–discharge (GCD), and electrochemical impedance spectroscopy (EIS). The electrochemical (EC) performance of the AGL-modified electrodes, fabrication of the asymmetric SCs, and calculation of the specific capacitance (C_{sp}), energy density (ED), and power density (PD) are discussed in detail below.

2.1.1. EC Performance of Mn_{AGL}@400-Modified Nickel Foam (Mn_{AGL}@400/Nickel Foam (NF)) Electrode

A series of EC studies were conducted to evaluate the suitability of Mn_{AGL}, Mn_{AGL}@200, Mn_{AGL}@400, and Mn_{AGL}@550 as electrode resources for SC applications. In the study of the performance of any SC, the foremost requirement is to access the cyclic voltametric aspects (which decode the nature of charge transfer, either surface- or diffusion-controlled pathways) of the materials modified onto the electrodes. The CV results were obtained within the potential range of 0–0.5 V vs. Ag/AgCl (filled with saturated potassium chloride (KCl)) at scan rates ranging from 5 to 200 mV/s. Furthermore, GCD measurements were performed at various current densities ranging from 1 to 20 A/g in the potential range of 0–0.5 V vs. Ag/AgCl. Additionally, the EIS techniques were measured at an open-circuit voltage from a frequency range of 10^{-2}–10^{5} Hz at an amplitude of 5 mV.

The specific capacitance (C_{sp}, F/g) was calculated as follows:

$$C_{sp} = \frac{i \times \Delta t}{\Delta V \times m} \quad (1)$$

where i, Δt, ΔV, and m denote the discharge current (A), discharge time (s), potential window (V), and mass of the active material, respectively.

2.1.2. Fabrication of Mn_{AGL}@400-Based Asymmetric SC

An asymmetric supercapacitor (ASC) device was constructed using a two-electrode cell with a 3 M potassium hydroxide (KOH) electrolyte. Mn_{AGL}@400 and activated carbon (AC) were modified on nickel foam and designated as the positive and negative electrodes, respectively. According to charge theory (where $q^+ = q^-$), confirming the mass balance between the positive and negative electrodes is essential. Hence, by balancing the charge stored between the positive and negative electrodes, the mass ratio can be calculated using the following equation:

$$\frac{m_+}{m_-} = \frac{C_{s-}\ \Delta V_-}{C_{s+}\ \Delta V_+} \tag{2}$$

where subscripts "+" and "−" denote the positive and negative electrodes, respectively.

The AC electrode prepared using the abovementioned method after mass balancing was mixed with 10 wt.% carbon black and 5 wt.% poly (vinylidene fluoride) (PVDF) and N-methyl pyrrolidone (NMP) as a mixing solvent to obtain a slurry, which was mixed with an agate motor to form a consistent colloidal paste. This well-mixed colloidal paste was coated onto the nickel foam (NF), with the electrodes being dried overnight in a vacuum oven at 60 °C. The activated carbon electrodes were designated as the negative electrodes in the asymmetric hybrid SC device.

2.1.3. Calculation of C_{sp}, ED, and PD

C_{sp} of the assembled hybrid device was calculated using Equation (1) by replacing "m" with "M"; M denotes the active mass of both positive and negative electrodes. Furthermore, the energy and power densities of Mn_{AGL}@400/NF were calculated using the following equations [29]:

$$\mathrm{ED} = \frac{C_s \times \Delta V^2}{2} \tag{3}$$

$$\mathrm{PD} = \frac{E}{\Delta t} \tag{4}$$

As mentioned earlier, ED and PD denote the energy (Wh/kg) and power (W/kg) densities of the asymmetric device, respectively; ΔV is the potential window from 0–1.65 V; C is the specific capacitance (C_{sp}, F/g) of the asymmetric device; Δt is the discharge time in seconds. A numerical value of 3600 was applied to convert the unit of time from seconds to hours while calculating ED and PD.

3. Results and Discussion

The HR-SEM images of the as-synthesized and annealed samples of Mn_{AGL}, Mn_{AGL}@200, Mn_{AGL}@400, and Mn_{AGL}@550 are shown in Figure 1a–d, which illustrate that the Mn_{AGL} sample displays highly uniform networked flower-like structures with accumulated NPs. The moisture content in as-synthesized Mn_{AGL} samples was removed when the annealing process started; however, at 550 °C, the small-sized Mn particles combined to form microparticles and almost lost their network structures. Interestingly, Mn_{AGL}@400 contained small Mn particles in network-like structures with observable porosity. The interaction of the electrolyte ions with the network of flower-like structures facilitates effortless charging and discharging processes. An even nanowafer-like morphology is also important for energy-related applications [30].

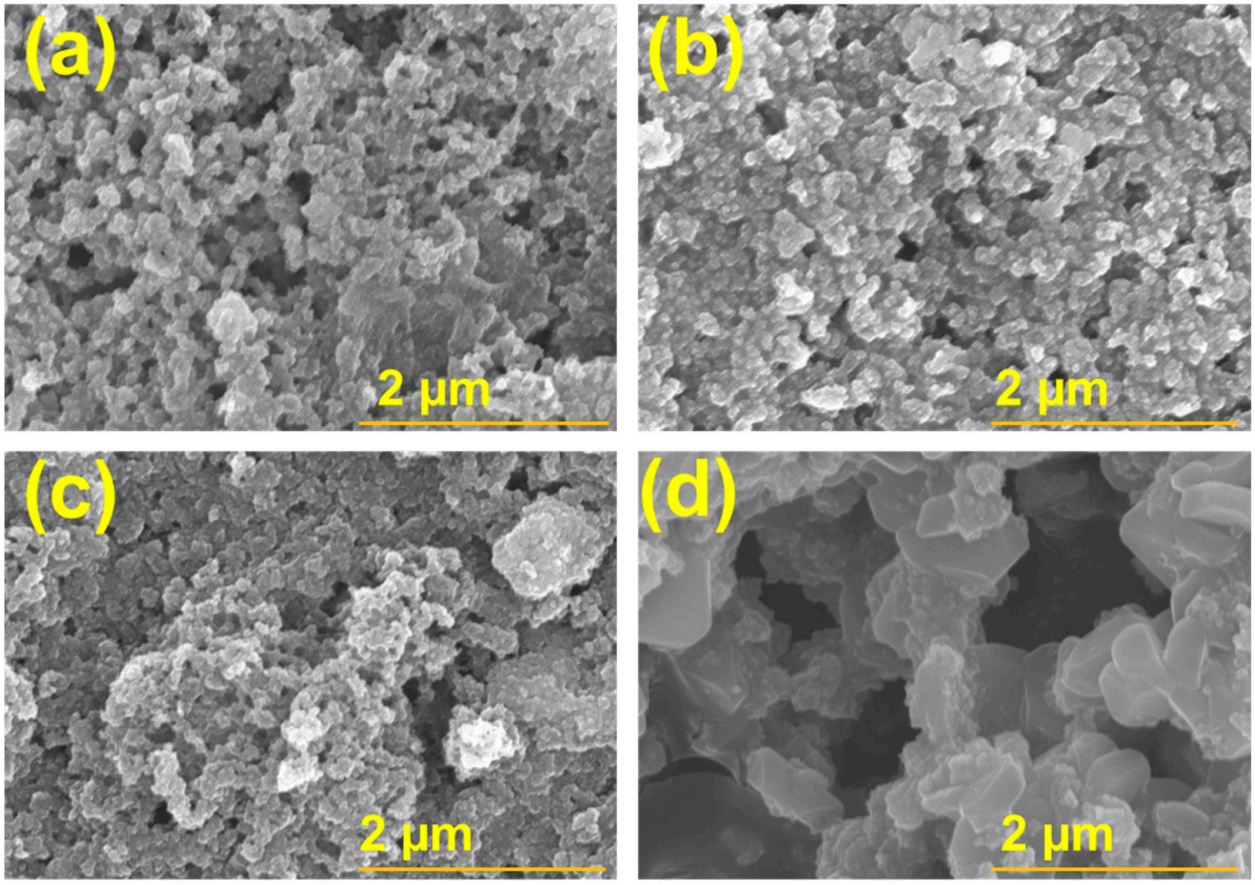

Figure 1. HR-SEM images of (**a**) Mn_{AGL}, (**b**) Mn_{AGL}@200, (**c**) Mn_{AGL}@400, and (**d**) Mn_{AGL}@550 at a magnification of 25×.

Figure 2a,b show the X-ray diffraction (XRD) and Fourier-transform infrared (FT-IR) spectra of the as-prepared Mn_{AGL} and annealed Mn_{AGL}@200, Mn_{AGL}@400, and Mn_{AGL}@550 samples, respectively. The XRD data confirmed the successful synthesis of Mn_{AGL}. As the annealing temperature increased, the amorphous AGLs became crystalline, similar to the usual nature of the AGLs. The XRD data of Mn_{AGL}@550 revealed several differently sized particles for the Mn_{AGL}@550 sample; however, the typical size of the particles was approximately 10–50 nm. Moreover, the finer and sharper nature of the XRD peaks for Mn_{AGL}@550 indicate the enhanced crystallinity of the annealed sample. The other samples exhibited an amorphous nature, while Mn_{AGL}@550 exhibited a clear, sharp nature with predominant peaks of MnO and Mn_2O_3 [31]. Owing to the generic amorphous nature of AGLs, the results are inconclusive in their observation of only the broad XRD peaks [32]. The JCPDS card numbers used for MnO and Mn_2O_3 were (07-0230) and (24-0508), respectively. A further detailed investigation with X-ray photoelectron spectroscopy (XPS) was conducted to ascertain the structures, chemical states, and valence states of the AGLs. The proposed synthesis strategy involves a one-pot method for producing Mn_{AGL} particles—one which is employable for diverse applications.

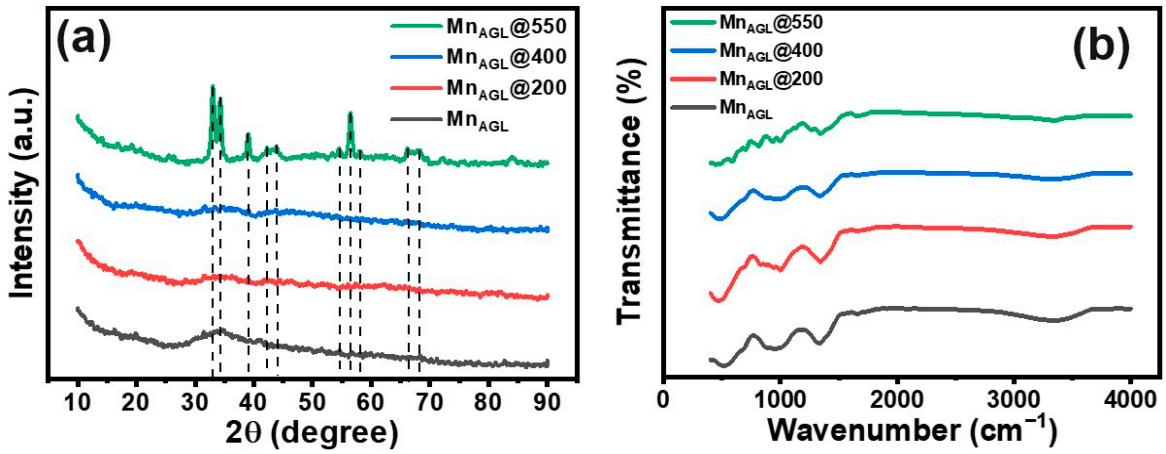

Figure 2. (**a**) XRD patterns and (**b**) FT-IR spectra of Mn_{AGL}, Mn_{AGL}@200, Mn_{AGL}@400, and Mn_{AGL}@550 samples.

FTIR spectra of the as-prepared Mn_{AGL} and annealed Mn_{AGL}@200, Mn_{AGL}@400, and Mn_{AGL}@550 samples are shown in Figure 2b. The broad peak located at ~3500 cm^{-1} indicates the occurrence of hydroxide (OH) stretching vibrations of physisorbed H_2O in all AGL samples. The weak peak at ~2275 cm^{-1} indicates the incidence of carbon dioxide (CO_2) in the sample, probably originating from peripheral adsorption. Notably, the peak at ~1656 cm^{-1} characterizes the bending vibration mode of water molecules. The peak at ~1329 cm^{-1} denotes O-H deformation—which was also observed in all AGL samples. The signature or fingerprint for the Mn-O stretching vibration peaks appeared in all the AGL samples, in the region between 517–558 cm^{-1} and 637–683 cm^{-1} [33]

XPS analysis was performed on the as-synthesized Mn_{AGL} and all annealed AGL samples—Mn_{AGL}@200, Mn_{AGL}@400, and Mn_{AGL}@550—to deduce the chemical configuration and valence states of each element. The XPS survey spectra of Mn_{AGL} and all annealed samples are shown in Figure S1 in the Supporting Information. Figure 3a–d show the Mn 2p spectra, while Figure 3e–h show the O 1s spectra of the $Mn_{AGL,}$ Mn_{AGL}@200, Mn_{AGL}@400, and Mn_{AGL}@550 AGL samples. These spectra contained one spin-orbit peak, at ~642 eV for Mn $2p_{3/2}$ and ~654 eV for Mn $2p_{3/2}$; these were deconvoluted by fitting along with the typical satellite peaks of Mn [34]. The spin-orbit splitting, denoted by the difference in the binding energy values of the two levels, was 12 eV, which was consistent with that reported for Mn-based systems [35]. The characteristic peak positions and their natures indicate that Mn_{AGL} deconvoluted into Mn^{2+}, Mn^{3+}, and Mn^{4+} moieties, wherein the Mn^{3+} ratio was slightly higher than or almost equal to (in the case of Mn_{AGL}@400) that of the other two ions. The ratio of Mn^{3+} to Mn^{4+} ions must be sufficiently close to ensure good conductivity. The ratio of the Mn_{AGL}@400 confirmed the presence of MnO and Mn_2O_3 based on the shape, nature, and peak positions of the Mn and O moieties [34]. Table 1 shows the ratios of Mn^{2+}, Mn^{3+}, and Mn^{4+} ions in the deconvoluted XPS spectra, indicating the effect of Mn^{3+} on the AGL samples. The trivalent Mn in Mn_2O_3 undergoes various transitions, such as Mn^{4+}/Mn^{3+} and Mn^{3+}/Mn^{2+}—important factors in determining the redox reactions of AGL electrodes. The XRD results suggest tiny peaks, demonstrating the presence of MnO and Mn_2O_3; hence, the annealed sample may contain Mn_2O_3 (excess) and MnO (small). The O 1s XPS studies also reveal the presence of O vacancies with an enhanced O_γ peak in the annealed Mn_{AGL}@400 sample. O_α and O_β denote lattice oxygen and surface-adsorbed oxygen, respectively. Surface-adsorbed oxygen and carbon can be detected at up to 0.01 monolayers, making it extremely difficult to distinguish between adsorbed and chemical oxygen atoms in oxide materials. Methods used to determine this difference effectively may involve using low-energy electron diffraction (LEED), temperature-programmed desorption (TPD), and scanning tunneling microscopy (STM), among other techniques [36,37]. In contrast to other methods, the borohydride hydrolysis

technique employed for synthesizing AGLs can efficiently produce MnO/Mn_2O_3 AGLs with a good number of oxygen vacancies [14]. The inconclusive nature of the XRD data led to a detailed study of the XPS data, which concluded that the Mn_{AGL} and annealed samples were present as MnO/Mn_2O_3. Hence, XPS is an effective procedure to deduce the oxidation states and vacancies of the compounds. The XPS results revealed that Mn_{AGL}@400 has more oxygen vacancies than the other AGL samples, making it an excellent candidate for SC [15].

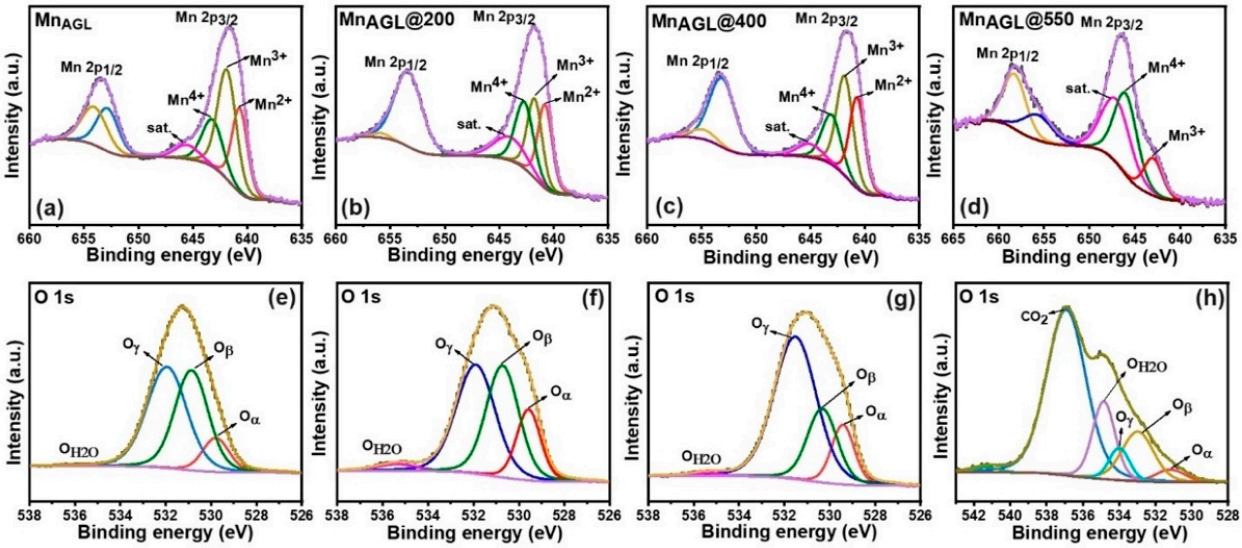

Figure 3. Deconvoluted XPS spectra of Mn 2p (**a**–**d**) and O 1s (**e**–**h**) for Mn_{AGL}, Mn_{AGL}@200, Mn_{AGL}@400, and Mn_{AGL}@550.

Table 1. Ratio of Mn^{2+}, Mn^{3+}, and Mn^{4+} ions from the deconvoluted XPS spectrum denoting the effect of Mn^{3+} on the AGL samples.

Deconvoluted Mn $2p_{3/2}$	Mn_{AGL}	Mn_{AGL}@200	Mn_{AGL}@400	Mn_{AGL}@550
2+	0.32	0.32	0.33	-
3+	0.38	0.37	0.34	0.44
4+	0.30	0.30	0.33	0.56

3.1. Electrochemical Studies

Electrochemical (EC) studies were conducted using 3M KOH as the electrolyte, with the working electrodes modified using the Mn_{AGL}, Mn_{AGL}@200, Mn_{AGL}@400, or Mn_{AGL}@550 samples. A comparison of the CV of all AGLs on the Ni foam electrodes is presented in Figure 4a. CV was conducted at varying scan rates ranging from 5 to 200 mV/s, with the current measured in the potential range of 0–0.5 V, as shown in Figure S2a–d. The reaction obeyed diffusion kinetics; hence, the square root of the scan rate vs. the peak current (Figure S2e–h) produced a straight line for all CV graphs with all AGL samples. These CV studies demonstrated the redox nature of Mn and the mesoporous structure of the AGL. Owing to the diffusion-controlled nature of the networked AGLs, with increasing scan rates, the peak current increased linearly but underwent a slight positive shift, possibly owing to the interruption of the mass transport reactions occurring at high scan rates. For instance, extremely low scan rates facilitate adequate interaction time between the OH^- ions from the electrolyte and the Mn^{4+}/Mn^{3+} and Mn^{3+}/Mn^{2+} ions accessible at the working electrode. However, at extremely high scan rates, the residence time is considerably reduced, resulting in broad peaks and positive potential shifts. All AGL-modified electrodes exhibited behaviors that fell under the category of battery-like materials with SC properties,

which resulted in definitive redox peaks but not rectangular Faradaic peaks, as observed in the CV studies. As explained earlier, the square root of the scan rate vs. the peak current plot is linear; hence, the reaction appears to follow diffusion-controlled kinetics [38]. Linear regression analysis was used to fit the square root of the scan rate versus the peak current for the Mn_{AGL}, Mn_{AGL}@200, Mn_{AGL}@400, and Mn_{AGL}@550 samples, with the values presented in Figure S2e–h. EC studies revealed the suitability of Mn_{AGL}@400 as a promising candidate for SC applications. The capacitance values for the three-electrode analysis are consistent with those in the literature available for Mn-based SCs and, considering the performance of an actual two-electrode device, the Mn_{AGL}@400 is in excellent agreement with previous studies. The C_{sp} values calculated from the CV curves at various scan rates from 5 to 200 mV/s, as shown in Figure 4c, were 31.4, 178, 230.8, and 132 F/g for Mn_{AGL}, Mn_{AGL}@200, Mn_{AGL}@400, and Mn_{AGL}@550, respectively. The capacitance values of the Mn_{AGL}@400 sample were the highest compared to those of the other AGL samples, indicating the suitability of Mn_{AGL}@400 as a unique and interesting material for energy-storage device applications.

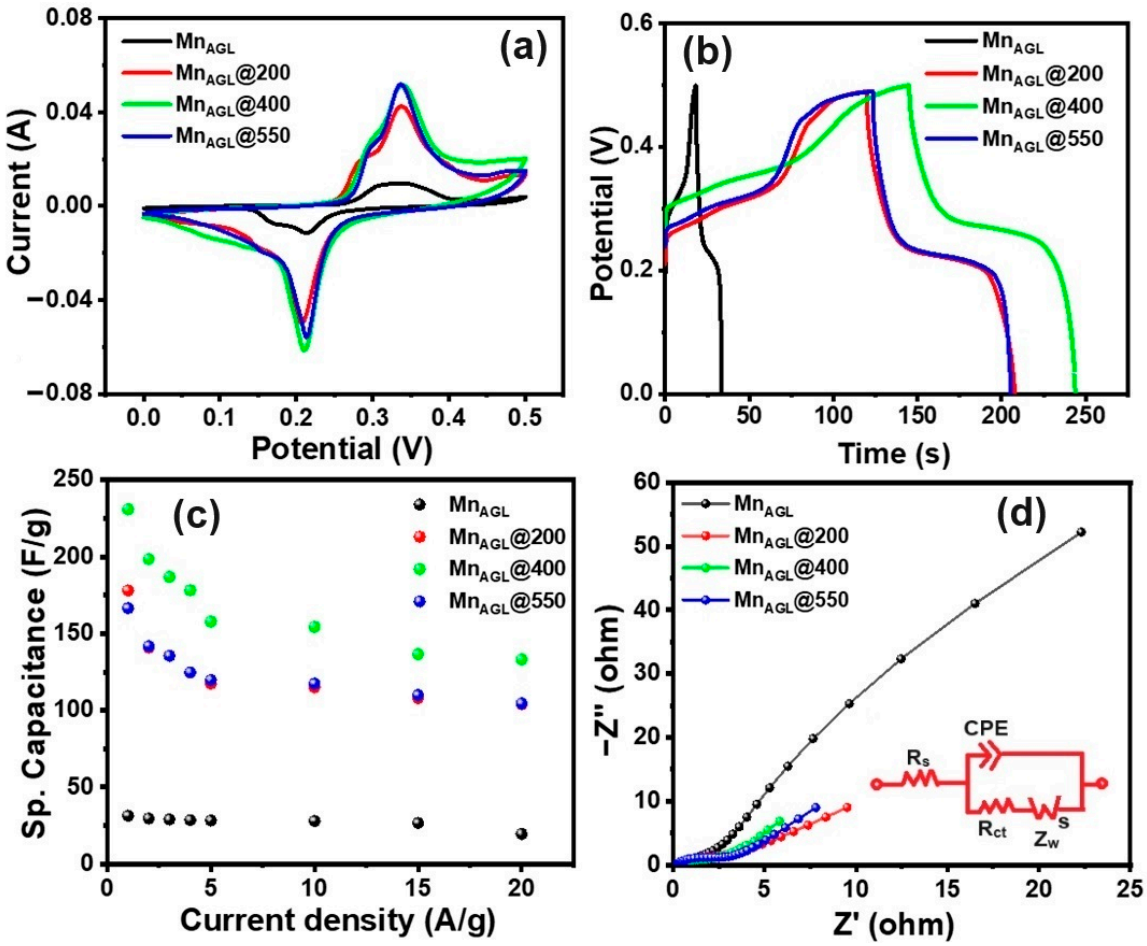

Figure 4. (**a**) CVs, (**b**) GCDs, (**c**) C_{sp} vs. current density plot, and (**d**) EIS graphs (inset: equivalent circuit) for Mn_{AGL}, Mn_{AGL}@200, Mn_{AGL}@400, and Mn_{AGL}@550 AGL samples.

3.2. Galvanostatic Charge–Discharge Studies

GCD experiments are similar to fingerprints in terms of calculating the actual and accurate capacitance of any electrode material. The Mn_{AGL}, Mn_{AGL}@200, Mn_{AGL}@400, and Mn_{AGL}@550 AGL materials were subjected to GCD measurements at CD values ranging from 1 to 20 A/g, as shown in Figure 4b. The relationship between C_{sp} and CD is shown in Figure 4c. Charge storage occurs in Mn AGLs by a redox mechanism between Mn^{3+} and Mn^{4+} ions via four different processes: surface chemisorption, intercalation or deinter-

calation of electrolyte cations, charge compensation, and tunnel storage. In this case, the Mn AGL exhibited capacitive properties owing to the intercalation/deintercalation of K^+ ions from the alkali hydroxide electrolyte, suggesting a diffusion-controlled mechanism. During charging, Mn^{3+} was oxidized to Mn^{4+}, while the reverse occurred during discharging [39,40]. Observing the nature of the charge–discharge curves for all the AGL-modified electrodes revealed battery-type behavior—characteristic of Mn-based electrode materials, as shown in Figure 4a,b. The typical charge–discharge curves for Mn-based systems exhibit a symmetric charge–discharge pattern with a low iR drop and a curved bend at approximately half the potential values—characteristic of battery-type capacitors and also exhibited by the proposed Mn-AGL-based electrodes. Furthermore, the enhanced discharge time indicates that Mn_{AGL}@400 performs better than the other AGL-modified electrodes. The C_{sp} values at various CDs (1, 5, 10, 15, and 20) for Mn_{AGL}@400 were 230.8, 157.8, 154.3, 136.5, and 133.21 F/g, respectively, while for the other AGL samples, their respective specific capacitance was much smaller when compared with the Mn_{AGL}@400 samples. The GCD graphs for all the AGL samples (Mn_{AGL}, Mn_{AGL}@200, Mn_{AGL}@400, and Mn_{AGL}@550) at various current densities are shown in Supplementary Information Figure S3a–d. These GCD studies revealed that reasonable C_{sp} values were possible even at high CD values, thus accentuating the stable nature and Faradaic qualities of the AGL-modified electrode materials. The IR drop for all AGL-modified electrodes was nearly the same; the value at 1 A/g CD was ~0.02 V. Table 2 shows the comparison data for Mn_{AGL}@400 electrodes: C_{sp}, ED, and PD values for Mn-based materials, based on previous reports.

Table 2. Comparison of Mn_{AGL}@400 electrodes: C_{sp}, ED, and PD values for Mn-based materials, based on previous reports.

Electrode	Electrolyte	C_{sp} (F/g@1 A/g)	ED (Wh/kg)	PD (W/kg)	Ref.
MnO_2/CA	6M KOH	170	8	3000	[16]
Mn_2O_3/n-CA/CN	1M Na_2SO_4	275	23	600	[17]
CNF/MnOx	1M Na_2SO_4	269 (5 mV/s)	37	2750	[18]
MnO_2/rGO	0.5M Na_2SO_4	63	18	400	[19]
Lignin/Mn-CA	6M KOH	186	-	-	[20]
Mn_2O_3/MnO_2	1M Na_2SO_4	225	27	90	[6]
Mn_2O_3	1M Na_2SO_4	209	29	250	[21]
MnO_2 NT	1M KOH	243	-	-	[22]
CTAB-Ag-MnOx	Na_2SO_4/$NaHCO_3$	145	-	-	[23]
MnOx-CDGs	1M Na_2SO_4	280	19	15,630	[24]
V-Mn-O//Zn ion	6M KOH/0.2M$(CH_3COO)_2$	333	150	900	[25]
MnO_2/N-rGO	0.5M Na_2SO_4	467	40	39	[26]
MnO_x/rGO_{ae}	1M Na_2SO_4	240	11	286	[27]
Mn_{AGL}@400	3M KOH	230.8	9.8	16,523	This work

CA, carbon aerogel; CN, cellulose nanofibrils; CNF, carbon nanocellulose fibers; NT, nanotubes; CTAB, cetyl trimethyl ammonium bromide; CDG, carbon dot/graphene nanocomposites; rGO_{ae}, reduced graphene oxide aerogel.

3.3. Electrochemical Impedance Spectroscopic Studies

The EIS measurements of the Mn_{AGL}, Mn_{AGL}@200, Mn_{AGL}@400, and Mn_{AGL}@550 AGL samples shown in Figure 4d are consistent with the GCD results. The solution resistance (R_s) for all samples accounted for 0.16 Ω, respectively. The charge-transfer resistance (R_{ct}) for Mn_{AGL}@400 was the least, measured at 2.5 Ω. Only Mn_{AGL}@400 and Mn_{AGL}@550 exhibited definitive R_{ct} values, whereas the others exhibited either plain straight lines or distorted semicircles. Based on the R_{ct} values, we conclude that the Mn_{AGL}@400 sample is a better candidate than the other Mn-based AGL electrodes. The inherent capacitive nature of these AGL electrode materials was revealed in the low-frequency data with a straight line or a linear response. However, Warburg-like behavior was observed for AGL samples at extremely low frequencies (0 Hz or less). A modified

Randles circuit including a Warburg and CPE, along with two resistors, was used to fit all the Nyquist data [30].

3.4. Device Fabrication

The real-world application of Mn_{AGL} electrodes was performed by constructing an asymmetric capacitor device with Mn_{AGL}@400/NF as the positive electrode and AC/NF as the negative electrode. This technique, employing one-pot sol–gel borohydride hydrolysis resulted in Mn_{AGLs} with better physical and electrochemical properties, making them suitable candidates for SC applications. The technique involving mass balance for the negative electrodes, as explained earlier, was performed by substituting the capacitance values of the AC at a particular mass and the capacitance of the positive electrode into Equation (2). Figure 5a shows the CV studies conducted at scan rates ranging from 5 to 100 mV/s, showing the redox peaks emerging from Mn in the positive electrode. Even though Mn_{AGL} exhibited battery-like behavior, the device showed few to no peaks owing to the effect of AC acting as a negative electrode. The effect of varying the potential limit versus current is shown in Figure 5b. In this plot, we can observe that a peak appears only for 1.65 V potential limits, possibly owing to the oxygen evolution reactions at higher voltages.

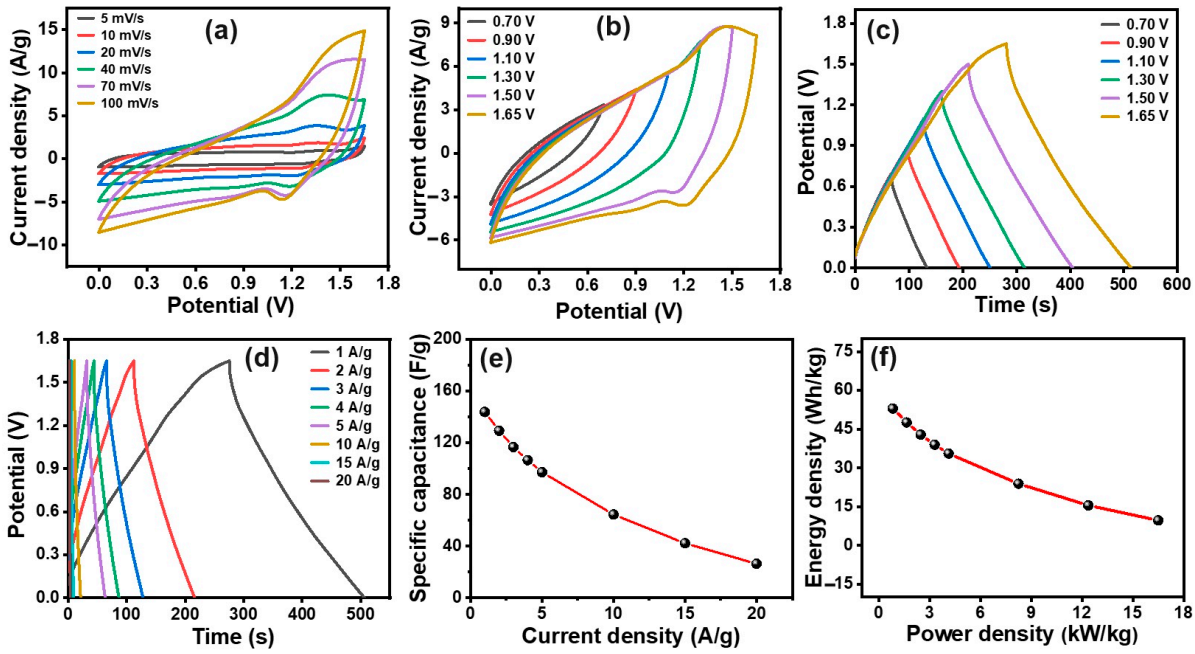

Figure 5. (**a**,**b**) CVs at various scan rates and various potential limits at 50 mV/s; (**c**,**d**) GCDs with various potential limits at 1 A/g and various current densities; (**e**) C_{sp} vs. current density plot; and (**f**) Ragone plot for Mn_{AGL}@400/NF//AC/NF device.

Figure 5c shows the GCD results at current densities ranging from 1 to 20 A/g. Based on the nature of the GCD studies, we also confirmed the battery-like behavior of Mn-related materials, especially Mn_{AGL}@400. GCD measurements were performed at different potential limits, as shown in Figure 5d. While increasing the potential limits from 0.7 V to 1.65 V, the discharge and charging times increased linearly. The C_{sp} values calculated for the CDs at 1, 3, 5, 10, and 20 A/g were 143.8, 116.6, 97.2, 64.4, and 26.3 F/g, respectively, as shown in Figure 5e. The real-time operation of any capacitor device depends on the results of CD studies. All data for the Nyquist plots in the EIS were obtained at an open-circuit voltage for the three-electrode device. The impedance values measured for the AGL device before (R_s) and after cycling (R_{ct}) stability measurements were 2.9 and 2.3 Ω and 37.6 and 4.2 Ω, respectively. The charge-transfer resistance decreased with cycling in the asymmetric device, possibly owing to the higher wettability of the electrode surface and the interaction

of OH^- ions in the open pores of the AGL structures. The large change in R_{ct} indicates that the stability of the device increased after cycling owing to the highly porous interconnected nature of the AGLs. In addition, the same modified Randles circuit shown in the inset of Figure 4d was employed to fit the data for the asymmetric device. Table 2 compares the C_{sp}, ED, and PD (Ragone plot depicted in Figure 5f) of the proposed AGL material with those of other SCs with similar electrode materials. The Mn AGLs are soft, fluffy materials prone to damage under harsh conditions. In contrast, based on the electrochemical performance of Mn_{AGL}@400 by CV and GCD measurements, the proposed materials are stable up to 550 °C. This study also confirms that the annealed AGL Mn_{AGL}@400 performs better than the other AGLs in all electrochemical studies, owing to the aforementioned reasons. Previous studies using Co AGLs have also confirmed this finding [30]. Figure S4a,b in the Supporting Information show the EIS of the device before and after cycling, as well as the cycling stability of the device for the Mn_{AGL}@400/NF//AC asymmetric capacitor, depicting the Coulombic efficiency and capacitance retention for 20,000 cycles.

Device performance depends to a considerable degree on key factors such as power and energy densities during the construction of ASCs. In the Ragone plot shown in Figure 5f, the performance of the Mn_{AGL}@400 device was compared with that of several Mn-based SCs. The ED and PD for a MnO_2/CA based system in a 6M KOH was 8 Wh/kg and 6 kW/kg at a current density of 0.5 A/g, while a Mn_2O_3/n-CA/CN modified electrode yielded 23 Wh/kg and 600 W/kg at a current density of 0.5 A/g, respectively. When CNF/MnOx was modified with NP in a 1M Na_2SO_4 electrolyte, the ED and PD values were 37 Wh/kg and 2.8 kW/kg. When researchers added to the MnO_2 moiety in a 0.5 M Na_2SO_4 electrolyte, the ED and PD values were 18 Wh/kg and 400 W/kg, respectively. Mn_2O_3/MnO_2-modified electrodes in 1M Na_2SO_4 exhibited ED and PD values of 27 and 90 W/kg, respectively. Mn_{AGL}@400 exhibited admirable ED and PD compared to other Mn-based electrodes reported in the literature. The main features of the Mn_{AGL}@400 modified electrode were its ultralow density, porosity, and excellent capacity, making it a promising contender as a lightweight electrode material for energy storage applications. In conclusion, with exceptional electrochemical results and power density values, the Mn_{AGL}@400-based SC offers excellent potential for energy storage in large-scale industrial applications.

4. Conclusions

In conclusion, Mn_{AGL} and its annealed AGL samples were efficiently synthesized using a one-pot sol–gel-based method employing cheap precursors and an efficient borohydride hydrolysis method. All Mn_{AGLs} exhibited flower-like assemblies containing a network of Mn and had moderate porosities. XRD data indicated the amorphous nature of all of the AGLs, except for Mn_{AGL}@550, which exhibited MnO/Mn_2O_3 polycrystalline sites. All AGL samples were subjected to electrochemical analyses, yielding C_{sp} values of 31.4, 178, 230.8, and 166.4 F/g, respectively for Mn_{AGL}, Mn_{AGL}@200, Mn_{AGL}@400, and Mn_{AGL}@550 modified electrodes in a three-electrode system. Hence, an ASC was constructed with Mn_{AGL}@400 and AC, yielding a C_{sp} of 143 F/g at 1 A/g. From the Ragone plot an *ED* and *PD* of 9.8 Wh/kg and 16,523 W/kg were obtained from the Ragone plots. The cycling stability of the asymmetric capacitor was evaluated for 20,000 cycles, with the results indicating a high-capacity retention of 97.3% with a Coulombic efficiency of 109%. Moreover, the combined effect of the borohydride hydrolysis strategy and lightweight AGL morphology facilitates the development of favorable ultralight SCs, making them candidates well-suited for meeting the ever-increasing energy needs of the future.

Supplementary Materials: The following supporting information can be downloaded at: https://www.mdpi.com/article/10.3390/en17102258/s1, Figure S1. XPS survey of Mn_{AGL}, Mn_{AGL}@200, Mn_{AGL}@400, and Mn_{AGL}@550 aerogel samples. Figure S2. (a–d) CV curves for the Mn_{AGL}, Mn_{AGL}@200, Mn_{AGL}@400, and Mn_{AGL}@550 aerogel samples at scan rates of 5–200 mV/s and their corresponding (e–h) scan rates vs. current density plots. Figure S3. (a–d) GCD graphs of the Mn_{AGL}, Mn_{AGL}@200, Mn_{AGL}@400, and Mn_{AGL}@550 aerogel samples at various current densities. Figure S4. (a) EIS graphs of Mn_{AGL}@400 before and after cycling (inset: enlarged view) and (b) cycling stability indicating

capacity retention and Coulombic efficiency of the device using Mn_{AGL}@400//NF aerogel samples and AC//NF electrodes.

Author Contributions: Conceptualization, R.R.; methodology, R.R.; software, R.R.; validation, R.R. and S.S.; formal analysis, R.R., J.P. and A.M.; investigation, R.R. and S.S.; resources, J.-J.S.; data curation, R.R., S.S. and A.M.; writing—original draft preparation and visualization, R.R.; table of content, S.S.; writing—review and editing, W.K.K.; supervision, T.H.O. and W.K.K.; project administration, W.K.K.; funding acquisition, J.-J.S. and W.K.K. All authors have read and agreed to the published version of the manuscript.

Funding: This work was supported by the National Research Foundation (NRF) of the Republic of Korea under the framework of the Consolidator Grant Program (NRF-2023R1A2C2007955), funded by the Ministry of Science and ICT, Republic of Korea.

Data Availability Statement: The original contributions presented in the study are included in the article/Supplementary Materials, further inquiries can be directed to the corresponding authors.

Conflicts of Interest: The authors declare no conflict of interest.

References

1. Nijsse, F.J.M.M.; Mercure, J.-F.; Ameli, N.; Larosa, F.; Kothari, S.; Rickman, J.; Vercoulen, P.; Pollitt, H. The Momentum of the Solar Energy Transition. *Nat. Commun.* **2023**, *14*, 6542. [CrossRef] [PubMed]
2. Fic, K.; Platek, A.; Piwek, J.; Frackowiak, E. Sustainable Materials for Electrochemical Capacitors. *Mater. Today* **2018**, *21*, 437–454. [CrossRef]
3. Khedulkar, A.P.; Dang, V.D.; Thamilselvan, A.; Doong, R.; Pandit, B. Sustainable High-Energy Supercapacitors: Metal Oxide-Agricultural Waste Biochar Composites Paving the Way for a Greener Future. *J. Energy Storage* **2024**, *77*, 109723. [CrossRef]
4. Lichchhavi; Kanwade, A.; Shirage, P.M. A Review on Synergy of Transition Metal Oxide Nanostructured Materials: Effective and Coherent Choice for Supercapacitor Electrodes. *J. Energy Storage* **2022**, *55*, 105692. [CrossRef]
5. Sakib, M.N.; Ahmed, S.; Rahat, S.M.S.M.; Shuchi, S.B. A Review of Recent Advances in Manganese-Based Supercapacitors. *J. Energy Storage* **2021**, *44*, 103322. [CrossRef]
6. Lu, W.; Li, Y.; Yang, M.; Jiang, X.; Zhang, Y.; Xing, Y. Construction of Hierarchical Mn_2O_3@MnO_2 Core–Shell Nanofibers for Enhanced Performance Supercapacitor Electrodes. *ACS Appl. Energy Mater.* **2020**, *3*, 8190–8197. [CrossRef]
7. Jiang, L.; Dong, M.; Dou, Y.; Chen, S.; Liu, P.; Yin, H.; Zhao, H. Manganese Oxides Transformed from Orthorhombic Phase to Birnessite with Enhanced Electrochemical Performance as Supercapacitor Electrodes. *J. Mater. Chem. A* **2020**, *8*, 3746–3753. [CrossRef]
8. Wei, W.; Cui, X.; Chen, W.; Ivey, D.G. Manganese Oxide-Based Materials as Electrochemical Supercapacitor Electrodes. *Chem. Soc. Rev.* **2011**, *40*, 1697–1721. [CrossRef] [PubMed]
9. Nechikott, A.A.; Nayak, P.K. Electrochemical Capacitance Properties of Pre-Sodiated Manganese Oxide for Aqueous Na-Ion Supercapacitors. *RSC Adv.* **2023**, *13*, 14139–14149. [CrossRef]
10. Zhu, S.; Li, L.; Liu, J.; Wang, H.; Wang, T.; Zhang, Y.; Zhang, L.; Ruoff, R.S.; Dong, F. Structural Directed Growth of Ultrathin Parallel Birnessite on β-MnO_2 for High-Performance Asymmetric Supercapacitors. *ACS Nano* **2018**, *12*, 1033–1042. [CrossRef]
11. Siddique, M.A.B.; Bithi, U.H.; Ahmed, A.N.; Gafur, M.A.; Reaz, A.H.; Roy, C.K.; Islam, M.M.; Firoz, S.H. Preparation of Manganese Oxide Nanoparticles with Enhanced Capacitive Properties Utilizing Gel Formation Method. *ACS Omega* **2022**, *7*, 48007–48017. [CrossRef] [PubMed]
12. Xiang, J.; Chen, J.; Zheng, Y.; Li, P.; Huang, J.; Chen, Z. Topological Design for Isotropic Metamaterials Using Anisotropic Material Microstructures. *Eng. Anal. Bound. Elem.* **2024**, *162*, 28–44. [CrossRef]
13. Tian, L.-Y.; Huang, P.-B.; Lv, J.-Q.; Zhang, Y.-H.; Zhao, L.-N.; Liu, L.; Wang, P.-F.; Wu, Y.-H.; Shi, Q.; Shi, F.-N. Metal-Organic Frameworks Based on Ternary Transition Metal Ions for High-Performance Lithium Ion Batteries. *J. Solid State Chem.* **2024**, *335*, 124717. [CrossRef]
14. Ramkumar, R.; Rajkumar, C.; Do, H.; Kim, H.; Kim, W.K. A Remarkable Oxygen Vacancy-Rich Rare Earth Aerogel with High Activity towards Electro and Catalytic Reduction of 5-Nitroquinoline. *J. Clean. Prod.* **2023**, *423*, 138683. [CrossRef]
15. Ramkumar, R.; Dhakal, G.; Tamang, T.L.; Yu, S.; Veerakumar, P.; Shim, J.-J.; Kim, W.K. Reverse-Engineered Borohydride Hydrolysis: Vacancy-Rich Cobalt Aerogel Nanowafers as High-Efficiency Electrode Materials for Supercapacitor Applications. *J. Energy Storage* **2024**, *86*, 111338. [CrossRef]
16. Xu, Y.; Wang, S.; Ren, B.; Zhao, J.; Zhang, L.; Dong, X.; Liu, Z. Manganese Oxide Doping Carbon Aerogels Prepared with MnO_2 Coordinated by N, N-Dimethylmethanamide for Supercapacitors. *J. Colloid Interface Sci.* **2019**, *537*, 486–495. [CrossRef] [PubMed]
17. Chen, Y.; Fang, L.; Hu, Y.; Lu, Y.; He, J.; Wang, S.; Yang, Q.; Shi, Z.; Xiong, C. Manganese Oxide/Nitrogen-Doped Carbon Aerogels from Cellulose Nanofibrils for High-Performance Supercapacitor Electrodes. *Diam. Relat. Mater.* **2022**, *122*, 108813. [CrossRef]
18. Guo, X.; Zhang, Q.; Li, Q.; Yu, H.; Liu, Y. Composite Aerogels of Carbon Nanocellulose Fibers and Mixed-Valent Manganese Oxides as Renewable Supercapacitor Electrodes. *Polymers* **2019**, *11*, 129. [CrossRef]

19. Qiu, X.; Xu, D.; Ma, L.; Wang, Y. Preparation of Manganese Oxide/Graphene Aerogel and Its Application as an Advanced Supercapacitor Electrode Material. *Int. J. Electrochem. Sci.* **2017**, *12*, 2173–2183. [CrossRef]
20. Xu, J.; Zhou, X.; Chen, M. Pore Structure Improvement of Lignin Composite Carbon Aerogels by Introducing Manganese Ion and Its Application in Supercapacitors. *Mater. Res. Express* **2019**, *6*, 065036. [CrossRef]
21. Chen, X.; Li, L.; Wang, X.; Xie, K.; Wang, Y. Effect of Manganese Valence on Specific Capacitance in Supercapacitors of Manganese Oxide Microspheres. *Chem. Eur. J.* **2021**, *27*, 9152–9159. [CrossRef] [PubMed]
22. Huang, M.; Zhang, Y.; Li, F.; Zhang, L.; Ruoff, R.S.; Wen, Z.; Liu, Q. Self-Assembly of Mesoporous Nanotubes Assembled from Interwoven Ultrathin Birnessite-Type MnO_2 Nanosheets for Asymmetric Supercapacitors. *Sci. Rep.* **2014**, *4*, 3878. [CrossRef]
23. Sun, Y.-A.; Chen, L.-T.; Hsu, S.-Y.; Hu, C.-C.; Tsai, D.-H. Silver Nanoparticles-Decorating Manganese Oxide Hybrid Nanostructures for Supercapacitor Applications. *Langmuir* **2019**, *35*, 14203–14212. [CrossRef] [PubMed]
24. Unnikrishnan, B.; Wu, C.-W.; Chen, I.-W.P.; Chang, H.-T.; Lin, C.-H.; Huang, C.-C. Carbon Dot-Mediated Synthesis of Manganese Oxide Decorated Graphene Nanosheets for Supercapacitor Application. *ACS Sustain. Chem. Eng.* **2016**, *4*, 3008–3016. [CrossRef]
25. Ashraf, I.; Abbas, Q.; Huang, Y.; Hassan, N.U.; Albaqami, M.D.; Tighezza, A.M.; Eldin, S.M.; Javed, M.S.; Ahmad, A.; Luque, R. V-Mn-O Aerogel Composite-Based High-Energy Zn-Ion Hybrid Supercapacitor. *J. Energy Storage* **2023**, *60*, 106601. [CrossRef]
26. Iamprasertkun, P.; Krittayavathananon, A.; Seubsai, A.; Chanlek, N.; Kidkhunthod, P.; Sangthong, W.; Maensiri, S.; Yimnirun, R.; Nilmoung, S.; Pannopard, P.; et al. Charge Storage Mechanisms of Manganese Oxide Nanosheets and N-Doped Reduced Graphene Oxide Aerogel for High-Performance Asymmetric Supercapacitors. *Sci. Rep.* **2016**, *6*, 37560. [CrossRef] [PubMed]
27. Suktha, P.; Chiochan, P.; Krittayavathananon, A.; Sarawutanukul, S.; Sethuraman, S.; Sawangphruk, M. In Situ Mass Change and Gas Analysis of 3D Manganese Oxide/Graphene Aerogel for Supercapacitors. *RSC Adv.* **2019**, *9*, 28569–28575. [CrossRef] [PubMed]
28. Boynuegri, T.A.; Gürü, M. Catalytic Dehydrogenation of Calcium Borohydride by Using Hydrogel Catalyst. *Int. J. Hydrogen Energy* **2017**, *42*, 17869–17873. [CrossRef]
29. Lakra, R.; Kumar, R.; Sahoo, P.K.; Sharma, D.; Thatoi, D.; Soam, A. Facile Synthesis of Cobalt Oxide and Graphene Nanosheets Nanocomposite for Aqueous Supercapacitor Application. *Carbon Trends* **2022**, *7*, 100144. [CrossRef]
30. Ramkumar, R.; Dhakal, G.; Shim, J.-J.; Kim, W.K. NiO/Ni Nanowafer Aerogel Electrodes for High Performance Supercapacitors. *Nanomaterials* **2022**, *12*, 3813. [CrossRef]
31. Stebounova, L.V.; Gonzalez-Pech, N.I.; Peters, T.M.; Grassian, V.H. Physicochemical Properties of Air Discharge-Generated Manganese Oxide Nanoparticles: Comparison to Welding Fumes. *Environ. Sci. Nano* **2018**, *5*, 696–707. [CrossRef] [PubMed]
32. Douk, A.S.; Farsadrooh, M.; Damanigol, F.; Moghaddam, A.A.; Saravani, H.; Noroozifar, M. Porous Three-Dimensional Network of Pd–Cu Aerogel toward Formic Acid Oxidation. *RSC Adv.* **2018**, *8*, 23539–23545. [CrossRef] [PubMed]
33. Amirtharaj, S.N.; Mariappan, M. Rapid and Controllable Synthesis of Mn_2O_3 Nanorods via a Sonochemical Method for Supercapacitor Electrode Application. *Appl. Phys. A* **2021**, *127*, 607. [CrossRef]
34. Sun, X.; Hao, Z.; Nan, H.; Xu, J.; Tian, H. Silver Decorated Lanthanum Calcium Manganate for Electrochemical Supercapacitor. *Mater. Res. Express* **2021**, *8*, 075502. [CrossRef]
35. Mahamad Yusoff, N.F.; Idris, N.H.; Md Din, M.F.; Majid, S.R.; Harun, N.A.; Noerochim, L. Coupling of Mn_2O_3 with Heteroatom-Doped Reduced Graphene Oxide Aerogels with Improved Electrochemical Performances for Sodium-Ion Batteries. *Nanomaterials* **2023**, *13*, 732. [CrossRef] [PubMed]
36. Pronin, I.A.; Averin, I.A.; Karmanov, A.A.; Yakushova, N.D.; Komolov, A.S.; Lazneva, E.F.; Sychev, M.M.; Moshnikov, V.A.; Korotcenkov, G. Control over the Surface Properties of Zinc Oxide Powders via Combining Mechanical, Electron Beam, and Thermal Processing. *Nanomaterials* **2022**, *12*, 1924. [CrossRef] [PubMed]
37. Komolov, A.S.; Lazneva, E.F.; Gerasimova, N.B.; Panina, Y.A.; Sobolev, V.S.; Koroleva, A.V.; Pshenichnyuk, S.A.; Asfandiarov, N.L.; Modelli, A.; Handke, B.; et al. Conduction Band Electronic States of Ultrathin Layers of Thiophene/Phenylene Co-Oligomers on an Oxidized Silicon Surface. *J. Electron Spectrosc. Relat. Phenom.* **2019**, *235*, 40–45. [CrossRef]
38. Bard, A.J.; Faulkner, L.R. *Electrochemical Methods: Fundamentals and Applications*, 2nd ed.; Wiley: New York, NY, USA; Weinheim, Germany, 2001; ISBN 978-0-471-04372-0.
39. Luo, S.; Shang, J.; Xu, Y.; Cheng, H.; Zhang, L.; Tang, Y. Stabilizing NiS_2 on Conductive Component via Electrostatic Self-assembly and Covalent Bond Strategy for Promoting Sodium Storage. *Adv. Funct. Mater.* **2024**, 2403166. [CrossRef]
40. Zhu, C.; Hao, Y.; Wu, H.; Chen, M.; Quan, B.; Liu, S.; Hu, X.; Liu, S.; Ji, Q.; Lu, X.; et al. Self-Assembly of Binderless MXene Aerogel for Multiple-Scenario and Responsive Phase Change Composites with Ultrahigh Thermal Energy Storage Density and Exceptional Electromagnetic Interference Shielding. *Nano-Micro Lett.* **2024**, *16*, 57. [CrossRef]